# Fast, semianalytical approach to obtain the stray magnetic field above a magnetic skyrmion

Alexandra R. Stuart,[1] Karen L. Livesey,[2] and Kristen S. Buchanan[1,*]
[1]*Department of Physics, Colorado State University, Fort Collins 80523, USA*
[2]*School of Information and Physical Sciences, University of Newcastle, Callaghan NSW 2308, Australia*

(Received 3 December 2021; accepted 15 April 2022; published 25 April 2022)

We present a fast, matrix-based semianalytical method to calculate the stray magnetic field and its derivative above spin textures with cylindrical symmetry. A magnetostatic Green's function approach is used to obtain accurate fields and magnetic forces, which are confirmed using micromagnetic simulations. The developed method can be used to quickly analyze and fit experimental measurements of the stray magnetic field (measured, for example, via nitrogen vacancies in diamond) or magnetic forces (measured via magnetic force microscopy) above a thin film or patterned element. Calculations for magnetic skyrmions show that these techniques have the potential to distinguish between Bloch and Néel walls for skyrmions in single-layer as well as in multilayer thin films where the wall structure evolves with depth.

DOI: 10.1103/PhysRevB.105.144430

## I. INTRODUCTION

Skyrmion spin textures are topologically protected spin states that are made up of a central, circular out-of-plane core with a bounding wall that can be Néel- or Bloch-type depending on the symmetry of the stabilizing Dzyaloshinskii-Moriya interactions. Skyrmions have recently attracted a great deal of attention due to their possible applications in spin-based electronics, and due to their potential to probe new physics [1–3]. Skyrmions can be stabilized in single-layer thin films, and multilayer films provide broader opportunities to modify the material properties in order to improve the room temperature stability of the skyrmions [4] and counter the skyrmion Hall effect [5]. Recently, it has been shown that the domain wall structure for a skyrmion in a multilayered film can be more complex than it is in a single magnetic layer, where the wall structure can evolve with depth from one chirality of Néel wall to the other, with a Bloch wall as an intermediate state [6]. Understanding the wall structure of skyrmions is critical for applications, and can also provide a means to probe the material properties. Moreover, the three-dimensional (3D) nature of spin textures, particularly how the spin textures evolve with depth, is, more generally, becoming increasingly important in magnetism [7].

X-ray-based techniques [8], especially tomography-based techniques, are leading to incredible advances in imaging of the internal 3D structure of complex materials [9] and depth-dependent spin structures, such as seen with magnetic skyrmions [10]. Lorentz transmission electron microscopy (LTEM) can also be used to obtain high resolution images of the magnetization state and to determine the skyrmion wall type, though the interpretation of measurements on structures with depth-dependent magnetization is more challenging [11,12]. Scanning probe techniques based on nitrogen vacancy (NV) centers in diamond [13–15] and magnetic force microscopy [16] are both important techniques for obtaining images of spin textures, and since these are tabletop techniques they offer the advantage that they are more accessible than synchrotron-based x-ray techniques or LTEM. Moreover, scanning probe techniques can be used to study samples that require specific substrates and that consequently cannot easily be grown directly on membranes. Modeling is, however, key to interpreting experimental data collected using these techniques since NV centers in diamond [17] and quantitative magnetic force microscopy (MFM) [18] both probe the magnetization state indirectly via measurements made above the sample surface. Both techniques hence rely on accurate calculations of the stray magnetic fields.

Much of the modeling work that has been done thus far to interpret scanning probe images of skyrmions has utilized full micromagnetic simulations. While micromagnetic simulations are unquestionably useful for capturing the details of skyrmions in real-world situations, simplified models are needed to link measurements done above a magnetic thin film to the spin texture that are both straightforward to use and also accurate. Analytical and semianalytical methods methods for obtaining the stray magnetic field and MFM contrast are valuable because unlike simulations, they provide a means to quantitatively fit experimental data to obtain the spin texture profile and, furthermore, to evaluate the associated uncertainties [19]. Analytical expressions derived using a multipole expansion have been used as an alternative to full simulations [18] but this approach only works well for pointlike skyrmions. Here we present an alternate method to obtain the stray magnetic field and the derivative of the stray magnetic field that MFM is sensitive to. We use magnetostatic Green's functions to derive expressions for the stray field components, and present a semianalytical matrix-based implementation of these expressions that can be used to fit experimental data for an arbitrary skyrmion magnetization profile. In fact, the stray field can be calculated for any other spin texture that has

*Kristen.Buchanan@colostate.edu

 

cylindrical symmetry, for example, vortices or more exotic quasiparticles including skyrmionium textures, and antiferromagnetic skyrmions [20] using this method. Our method is based on our previous work that used Green's function methods to evaluate the demagnetizing fields in textures with cylindrical symmetry [21] and that method is extended here to find the exact magnetic field produced *outside* the magnet with no approximations. Our expression provide a straightforward and accurate means to obtain the stray field above a spin texture with cylindrical symmetry, and the presented 1D matrix calculation method is significantly faster than using demagnetization kernel from a traditional 2D micromagnetic solver to find the stray field for a specified profile.

Of most interest to experimentalists is the possibility to take a measurement for the stray field or the MFM signal and find the underlying magnetization profile from this. Using micromagnetics, this can be a lengthy process because it typically involves obtaining relaxed spin distributions with a large number of cells for a variety of magnetic properties. Here, we show that it is possible to not only obtain the predicted stray field profile with the developed expressions and a matrix approach but also to find the best fit skyrmion parameters and detailed information about the uncertainties in those parameters in just a few seconds. This proof of principal calculation is done on synthetic data with a 10% noise added.

Section II outlines analytical expressions for the skyrmion magnetization profiles that will be used in the calculation of the stray field. The semianalytical approach is described in Sec. III, along with the micromagnetic simulations that were done to validate the matrix-based approach. The results section, Sec. IV, shows calculations of the stray field profiles for several representative cases and the close match between the matrix method approach and micromagnetic simulations. Approaches to the inverse problem of finding a magnetization profile from magnetic field measurements are discussed and demonstrated. A summary is provided in Sec. V.

## II. SKYRMION MAGNETIZATION MODELS

The skyrmion magnetization distribution, illustrated in Fig. 1 for a Néel skyrmion, has radial symmetry and the magnetization is constant along the film thickness. Hence, the problem can be reduced to a one-dimensional (1D) distribution $\mathbf{M}(r)$, where $r$ is the radial coordinate in a cylindrical coordinate system. The magnetization profile is parameterized in terms of the skyrmion radius $R_{\rm sk}$ and the skyrmion wall thickness $\Delta$, as indicated in Fig. 1(b). The skyrmion magnetization can be described using equation (3) of the supplemental materials of Ref. [22], a profile that is justified by experiments. Using $\rho_o = R_{\rm sk}/\Delta$, $\varrho = r/\Delta$, the magnetization angle with respect to the out-of-plane $z$ direction is

$$\theta(\rho_o, \varrho) = 2\text{atan}(\exp(\varrho - \rho_o)) + 2\text{atan}(\exp(\varrho + \rho_o)) - (\wp + 1)\frac{\pi}{2}, \quad (1)$$

where $\wp = \pm 1$ is the skyrmion polarization, i.e., the out-of-plane direction of the skymrion core. Equation (1) can be used to describe a skyrmion of Bloch, Néel, or mixed character by introducing a parameter $\psi$ to describe the in-plane magnetization angle. The out-of-plane normalized magnetization is

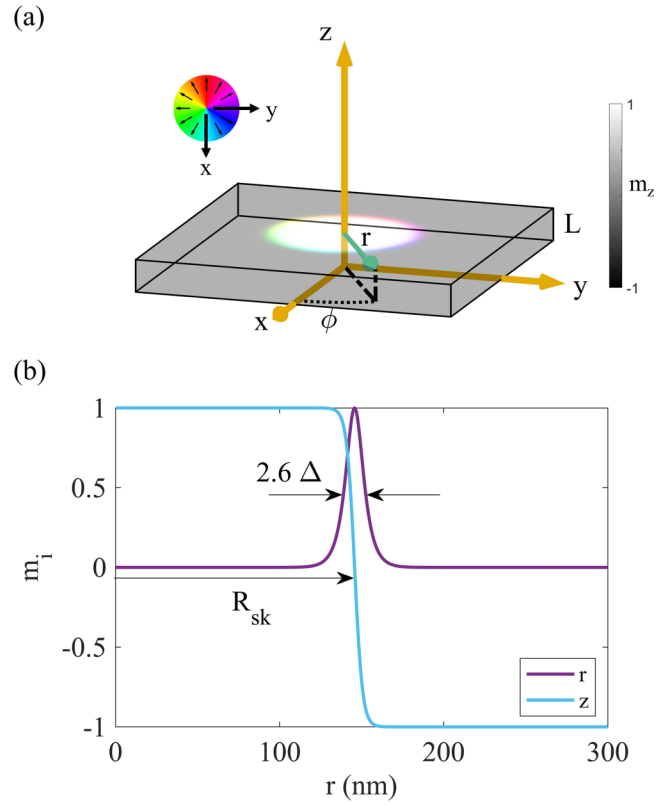


FIG. 1. (a) Diagram of a skyrmion with cylindrical symmetry in a single ferromagnetic layer of thickness $L$. The origin is at the bottom of the thin film. (b) Magnetization profile of a Néel skyrmion with $\psi = 0$, radius $R_{\rm sk} = 145.7$ nm, and $\Delta = 4.8$ nm from Eq. (1). The out-of-plane component (light blue) and the radial component (purple) are shown.

$m_z = M_z/M_s = \cos\theta$, and the in-plane radial and azimuthal components are $m_r = m_{ip}\cos\psi$ and $m_\phi = m_{ip}\sin\psi$, respectively, where $m_{ip}(\rho_o, \varrho) = \sqrt{1 - m_z^2}$ and all components of the magnetization are normalized by the saturation magnetization $M_s$. For a Néel wall that points radially outwards (inwards), $\psi = 0\ (\pi)$, whereas for a Bloch wall, $\psi = \pm\pi/2$. Figure 1(b) shows the magnetization profile of a representative Néel skyrmion with $\psi = 0$ and $\wp = 1$.

In our calculation of the stray field (Sec. III), the magnetization ansatz given in Eq. (1) is used, with $R_{\rm sk}$ and $\Delta$ values found via micromagnetic simulations for a given set of thin film parameters. For the analysis of experiments, $R_{\rm sk}$, $\Delta$ and $\psi$ would be used as fitting parameters, allowing micromagnetic simulations to be bypassed. In other words, matching the measured stray field to that which is calculated using the semianalytic approach allows one to obtain the skyrmion parameters. This will be explored more in Sec. IV.

## III. APPROACH

Calculating the stray magnetic fields above a skyrmion is challenging because the stray magnetic fields are long range. Stray magnetic fields arise from gradients of the magnetization that occur due to discontinuities in the magnetization, e.g., at the edges of a patterned structure, or due to smooth

gradients in the magnetization, for example at a domain wall or skyrmion boundary. The stray magnetic fields of a skyrmion will be strongest near its boundary but they are also generally non-negligible directly above the skyrmion and for some distance outside of the skyrmion wall. Here, we use a matrix-based implementation of a Green's function approach to obtain the stray magnetic field above a single skyrmion.

### A. Stray field

To obtain the stray magnetic field, we use the magnetostatic tensorial Green's function. The tensor components needed to calculate the internal demagnetization fields for cylindrical spin distributions were derived previously for the radial [21,23] and out-of-plane [21] directions, and we recently used these expressions to find the radial modes of a vortex with DMI [21]. In this section, we will derive the expressions for magnetic field above or below a magnetic skyrmion in a thin film of thickness $L$.

By symmetry, the magnetic field $\vec{H}$ inside and outside of the magnetic film will only have components in the $r$ and $z$ directions. However, the radial component of the magnetization contributes to both $r$ and $z$ components of $\vec{H}$, as does the $z$ component of the magnetization. The cross terms ($H_r$ due to $m_z$ and $H_z$ due to $m_r$) average to zero for the intralayer demagnetization field but are nonzero for the case of a stray field above or below the magnetic thin film. The magnetostatic tensorial Green's functions are defined as

$$\hat{\Gamma}(\mathbf{r},\mathbf{r}') = -\nabla\nabla' G(\mathbf{r},\mathbf{r}') \tag{2}$$

where $G = 1/(4\pi|\mathbf{r}-\mathbf{r}'|)$ is the Coulombic Green's function, and a form appropriate for a problem with cylindrical symmetry is [24]

$$G(\mathbf{r},\mathbf{r}') = \frac{1}{4\pi}\sum_{m=-\infty}^{\infty}\int_0^\infty dk\, J_m(rk)J_m(r'k) \times e^{im(\phi-\phi')}e^{-k|z-z'|}. \tag{3}$$

The reduced (unitless) magnetic field from a particular magnetization profile can be found at any position in space by integrating the Green's function tensor multiplied by the magnetization sources as follows:

$$\mathbf{h_d}(r,z,\phi) = \int_0^\infty dr' r' \int_0^{2\pi} d\phi' \int_{-\infty}^{\infty} dz'\, \hat{\Gamma}\mathbf{m}(r',z',\phi') \tag{4}$$

(in SI units; a prefactor of $4\pi$ appears for cgs units). The magnetization profile does not depend on the azimuthal coordinate $\phi'$ and we assume that it is constant through the thickness of the film. Furthermore, we expect the magnetic field to have no azimuthal dependence and magnetic material has radius $R$. With these assumptions, Eq. (4) simplifies to

$$\mathbf{h_d}(r,z) = \begin{pmatrix} h_{d,r} \\ h_{d,z}\end{pmatrix} = \int_0^R dr' r' \begin{pmatrix} g_{rr'} & g_{rz'} \\ g_{zr'} & g_{zz'}\end{pmatrix}\begin{pmatrix} m_{r'}(r') \\ m_{z'}(r')\end{pmatrix}, \tag{5}$$

where the simplified Green's function tensor components are

$$g_{\alpha\beta}(z,r,r') = \frac{1}{2\pi}\int_0^L dz' \int_0^{2\pi} d\phi \int_0^{2\pi} d\phi'\, \Gamma_{\alpha\beta}, \tag{6}$$

where $\alpha, \beta = r, z$.

The first of the four tensor components $g_{rr'}$ is

$$g_{rr'} = -\frac{1}{2}\int_0^\infty dk\, k^2 J_1(kr)J_1(kr')\int_0^L dz'\, e^{-k|z-z'|} = -\frac{1}{2}\int_0^\infty dk\, kJ_1(kr)J_1(kr')(e^{-k|z-L|} - e^{-k|z|}). \tag{7}$$

The expression above, and those that follow, involve integrals of the form

$$I(\mu,\nu;\lambda) = \int_0^\infty k^\lambda J_\mu(kr)J_\nu(kr')e^{-k\alpha}dk, \tag{8}$$

and these integrals have solutions that can be expressed in terms of elliptic integrals (see Ref. [25] for details). For $g_{rr'}$, the solutions is

$$g_{rr'}(z,r,r') = -\tfrac{1}{2}[v_{111}(|z-L|) - v_{111}(|z|)] \tag{9}$$

with

$$v_{111}(\alpha) = \frac{2\alpha}{\pi r r' \gamma_2(1-p^2)}\left[-K(p^2) + \frac{(1+p^2)}{(1-p^2)}E(p^2)\right], \tag{10}$$

where $K$ and $E$ are elliptic integrals of the first and second kind, respectively. The definitions of the lengths $\gamma_1$ and $\gamma_2$ are

$$\gamma_1 = \tfrac{1}{2}(\sqrt{(r+r')^2+\alpha^2} - \sqrt{(r-r')^2+\alpha^2}), \tag{11}$$

$$\gamma_2 = \tfrac{1}{2}(\sqrt{(r+r')^2+\alpha^2} + \sqrt{(r-r')^2+\alpha^2}), \tag{12}$$

and their ratio is

$$p = \gamma_1/\gamma_2. \tag{13}$$

In Eq. (10) and the equations that follow, we assume that the complete elliptic integrals are specified in terms of the parameter $m = p^2$, instead of the elliptic modulus $k = p$.

The next tensor component is

$$g_{zz'} = -\frac{1}{2}\int_0^\infty dk\, J_0(kr)J_0(kr')\int_0^L dz' \frac{\partial}{\partial z}\frac{\partial}{\partial z'}e^{-k|z-z'|}, \tag{14}$$

which is, in terms of elliptic integrals,

$$g_{zz'}(z,r,r') = \tfrac{1}{2}[v_{001}(|z-L|) - v_{001}(|z|)], \tag{15}$$

with

$$v_{001}(\alpha) = \frac{2\alpha}{\pi\gamma_2^3(1-p^2)}\left[-K(p^2) + \frac{2}{(1-p^2)}E(p^2)\right]. \tag{16}$$

Finally, the off diagonal components that are used to capture the $z$ ($r$) component of the stray magnetic field generated by $m_r$ ($m_z$) are

$$g_{rz'} = \frac{1}{2}\int_0^\infty dk\, kJ_1(kr)J_0(kr')\int_0^L dz' \frac{\partial}{\partial z'}e^{-k|z-z'|},$$

$$g_{zr'} = \frac{1}{2}\int_0^\infty dk\, kJ_0(kr)J_1(kr')\int_0^L dz' \frac{\partial}{\partial z}e^{-k|z-z'|}.$$

The solutions are

$$g_{rz'}(z,r,r') = \tfrac{1}{2}[v_{101}(|z-L|) - v_{101}(|z|)], \tag{17}$$

$$g_{zr'}(z,r,r') = -\tfrac{1}{2}[v_{011}(|z-L|) - v_{011}(|z|)] \tag{18}$$

with

$$v_{011}(\alpha) = \frac{2}{\pi r' \gamma_2^3 (1-p^2)}\left[\left(\gamma_2^2 - r'^2\right)K(p^2) - \frac{(\alpha^2 + r^2 - r'^2)}{(1-p^2)}E(p^2)\right], \tag{19}$$

$$v_{101}(\alpha) = \frac{2}{\pi r \gamma_2^3 (1-p^2)}\left[\left(\gamma_2^2 - r^2\right)K(p^2) - \frac{(\alpha^2 + r'^2 - r^2)}{(1-p^2)}E(p^2)\right]. \tag{20}$$

The expressions above are valid for $z > L$.

We pause to emphasize that Eqs. (9), (15), (17), and (18), when substituted into Eq. (5), allows the calculation of the stray field above a skyrmion or any magnetic texture with cylindrical symmetry. The matrix components $g_{\alpha\beta}$ are semianalytic since they involve elliptic functions. The stray field calculation at a given position is reduced from a two-dimensional integral over a film to a one-dimensional integral along the radial component. To find the stray field below the thin film, the sign is the same for $g_{rr'}$ and $g_{zz'}$, whereas the signs flip for $g_{rz'}$ and $g_{zr'}$.

The stray field integral [Eq. (5)] must be evaluated numerically, however, this can be set up as a matrix-based calculation so that the calculations are fast and can be used to fit experimental data. In fact, we find that the stray field can be predicted significantly faster this way than through micromagnetic simulations (see Appendix B for details), where this time saving is associated with the stray field calculation step. Micromagnetic simulations also require a longer initial calculation of the kernel, and if the spin distribution is relaxed then it can take minutes or hours for a single stray field calculation. We recently used such a matrix approach for a magnetic texture with cylindrical symmetry to find dynamical modes [21]. The continuous magnetization profile [Eq. (1)] and Green's function tensor are discretized into steps of size $\delta'$, where $\delta'$ is chosen to be small compared to the spatial variation of the magnetization along the radial direction. The vector stray field is

$$\mathbf{h_d}(r, z) = \hat{G}_d \mathbf{m}(r'), \tag{21}$$

where $\hat{G}_d$ is the magnetostatic, tensorial, nonlocal, integral matrix operator

$$\hat{G}_d = \begin{bmatrix} \hat{A}_{rr'} & \hat{A}_{rz'} \\ \hat{A}_{zr'} & \hat{A}_{zz'} \end{bmatrix}. \tag{22}$$

The tensor sub components are

$$\hat{A}_{\alpha\beta'} = \hat{g}_{\alpha\beta'} \cdot \mathrm{diag}(r') \cdot \delta', \tag{23}$$

where the nonlocal integral operators $\hat{g}_{\alpha\beta'}$ are discretized matrices (for more details see Appendix A), and $\mathrm{diag}(r')$ is a square matrix of dimension $(R/\delta')$, with the discrete distances $r'$ ranging from $\delta'$ to $R - \delta'/2$ on its diagonal and all other elements zero. The radius $R$ can be used to represent a finite-sized magnetic element, or a safe distance from the edge of a skyrmion that resides in an extended thin film (i.e., $R > R_{\mathrm{sk}} + 2\Delta$), the approach used in the examples that follow. The initial calculation of the matrix, which only needs to be done once for a given height $z$, takes a few seconds or less, and the subsequent evaluations of Eq. (21) take less than a millisecond for a typical calculation.

### B. MFM signal

The force on an MFM tip is proportional to $\partial h_{d,z}/\partial z$. This is a point dipole approximation, which is usually sufficient to compare to experimental data and also serves as the basis for models that account for the dipole nature of the tip. The derivatives of the relevant tensor components are

$$\frac{\partial g_{zz'}(r', z)}{\partial z} = \frac{1}{2}[v_{002}(|z|) - v_{002}(|z - L|)] \tag{24}$$

and

$$\frac{\partial g_{zr'}(r', z)}{\partial z} = -\frac{1}{2}[v_{012}(|z|) - v_{012}(|z - L|)] \tag{25}$$

with

$$v_{002}(\alpha) = \frac{2\left(\gamma_2^2(1-p^2)^2 - 5\alpha^2 - 3\alpha^2 p^2\right)}{\pi \gamma_2^5 (1-p^2)^3}K(p^2) - \frac{4\left(\gamma_2^2(1-p^2)^2 - 4\alpha^2(1+p^2)\right)}{\pi \gamma_2^5 (1-p^2)^4}E(p^2), \tag{26}$$

$$v_{012}(\alpha) = \frac{2\alpha\left(\gamma_2^2 + 7\gamma_1^2 - 5r'^2 - 3r'^2 p^2\right)}{\pi r' \gamma_2^5 (1-p^2)^3}K(p^2) + \frac{2\alpha\left(8r'^2(1+p^2) - p^2\gamma_1^2 - \gamma_2^2 - 14\gamma_1^2\right)}{\pi r' \gamma_2^5 (1-p^2)^4}E(p^2). \tag{27}$$

Expressed as a matrix calculation, the MFM signal is

$$\frac{\partial h_{d,z}}{\partial z} = \left[\frac{\partial \hat{A}_{zr'}}{\partial z} \cdot \frac{\partial \hat{A}_{zz'}}{\partial z}\right]\mathbf{m}(r'). \tag{28}$$

PYTHON code that implements the described methods to calculate the stray magnetic field and the MFM signal is included in Ref. [27].

### C. Micromagnetic simulations

Micromagnetic simulations were performed using MUMAX3 [26] to obtain stray field and MFM signal profiles to compare with the 1D matrix-based calculations. The simulations were conducted by relaxing a Néel skyrmion in zero magnetic field in a single magnetic layer of thickness $L = 1$ nm. Parameters similar to those of a Pt/Co/Ir trilayer film were used: $M_s = 1.1 \times 10^6$ A/m, $A_{ex} = 1.0 \times 10^{-11}$ J/m$^2$, a perpendicular magnetocrystalline anisotropy of $K_u = 1.15 \times 10^6$ J/m$^3$, and an interfacial DMI of $-2.1$ mJ/m$^2$. This leads to a relaxed Néel skyrmion that is stable at remanence. The magnetization profile [essentially identical to Fig. 1(b)], stray field, and MFM profiles were calculated and all exhibit cylindrical symmetry. The skyrmion radius was found to be $R_{\mathrm{sk}} = 145.7$ nm, which relaxed slightly to 136.8 nm for the simulations conducted to calculate the MFM profile, with a domain wall width of $\Delta = 4.8$ nm in both cases. These values were used in the semianalytic matrix method to predict the stray field above the skyrmion.

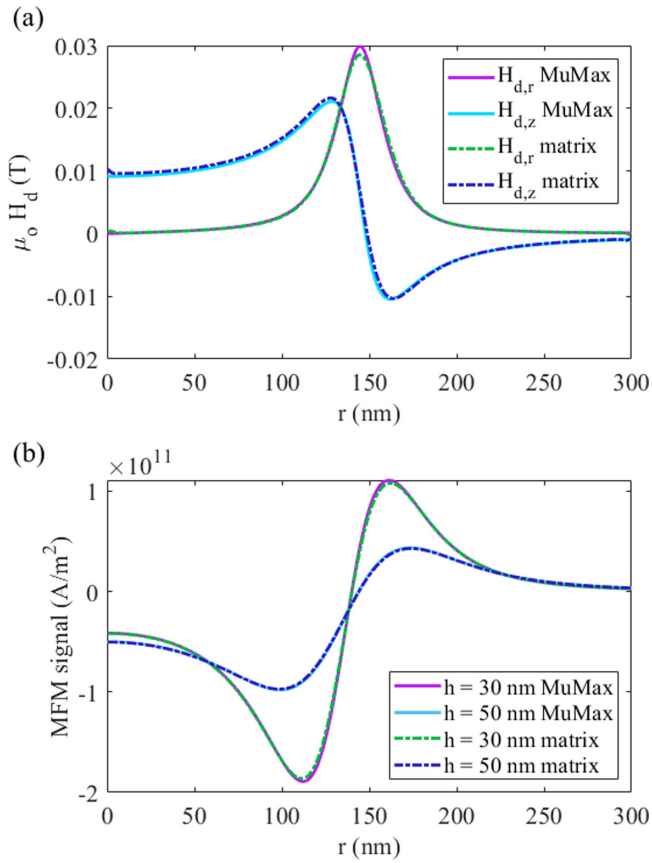


FIG. 2. Comparison of 1D (a) stray field and (b) MFM signal profiles extracted from fits to micromagnetic simulations, and from matrix-based calculations done using the two skyrmion fit parameters, $R_{sk}$ and $\Delta$, and the analytical magnetization profile [Eq. (1)]. The matrix calculations in (a) are at $h = 3.5$ nm and the simulations are averaged across a 1-nm-thick cell, centered at the same $h$ value. For (a) and (b), $R_{sk} = 145.7$ and 136.8 nm, respectively, and $\Delta = 4.8$ nm and $\wp = +1$ for both.

## IV. RESULTS

Firstly, we will compare the results of the semianalytical calculations to the MuMax results to validate the matrix approach. Secondly, we will explore the stray magnetic fields and expected MFM signals for two different scenarios: (i) Néel skyrmions of both chiralities and a Bloch skyrmion in a single layer and (ii) a multilayer skyrmion (in three layers) where the wall type evolves with depth. As shown in Ref. [6], the character of a skyrmion wall can evolve from Néel to Bloch types as a function of depth in multilayered films such that a vortex-type configuration is realized in a cross-sectional slice through the skyrmion wall. This reduces the net demagnetization energy of the skyrmion spin texture and can hence be energetically favorable if the exchange coupling between the magnetic layers is relatively weak.

Figure 2(a) shows 1D profiles of the stray field for $z = 4.5$ nm (that is at a height $h = z - L = 3.5$ nm above the film) obtained from MUMAX and calculated using the matrix method and the skyrmion magnetization profile shown in Fig. 1(b). Figure 1(b) shows the magnetization profiles generated using Eq. (1), which is almost indistinguishable from the magnetization extracted from the relaxed skyrmion from the MUMAX simulations, with $R_{sk}$ and $\Delta$ values given in the figure caption. Figure 2(b) shows the MFM signal at $h = 30$ and 50 nm. These results were calculated separately and the skyrmion relaxed slightly to a smaller radius of $R_{sk} = 136.8$ nm, which was used to calculate the MFM profiles. In Fig. 2, the matrix-based calculations agree very well with the MUMAX results. We note that the MUMAX MFM signal was scaled by a factor of 1/2, which reflects a difference in the definition of the MFM signal [the results shown in Fig. 2(b) match numerical calculations of $\partial h_{d,z}/\partial z$]. There is a slight discrepancy in the peak $H_{d,r}$ values, which is likely because the MUMAX stray field is averaged across a 1-nm-thick cell centered at height $h$, whereas the matrix method yields $\mathbf{h_d}$ at a specific $h$.

The matrix-based approach was used to examine several scenarios to illustrate the variation in the field and the MFM signals expected for problems of interests. First, a magnetic skyrmion in a Co thin film with $L = 1$ nm is considered. Here we have focused on larger bubble-type skyrmions so that the fields in the skyrmion center and above the skyrmion wall can be distinguished, but the method works equally well for smaller pointlike skyrmions. The stray magnetic fields above and below a skyrmion with $R_{sk} = 145.7$ nm and $\Delta = 4.8$ nm are shown in Fig. 3. The individual contributions $H_{d,rr}$ and $H_{d,rz}$ shown in panel (a) are the contributions to $H_{d,r}$ due to the $r$ and $z$ components of the magnetization, respectively, and $H_{d,zr}$ and $H_{d,zz}$ are similarly the contributions to $H_{d,z}$ due to $m_r$ and $m_z$, respectively. The contributions due to $m_z$ dominate, but for a Néel wall, the contributions from $m_r$ are also sizable.

For a Bloch wall, $m_r = 0$ so the magnitudes of $H_{d,r}$ and $H_{d,z}$ are the same above and below a Bloch skyrmion [see yellow dotted and blue dashed lines in Figs. 3(b) and 3(c)] and are independent of the skyrmion chirality, whereas for a Néel wall the fields above and below the skyrmion differ in magnitude by more than a factor of three (solid pink line and dot-dashed green line). The magnetic field at the center of the skyrmion is in the $z$ direction and has the same magnitude independent of the wall type (Bloch or Néel) for this large, bubble-type skyrmion. For smaller $R_{sk}$ values, the wall contributions will overlap with the skyrmion center and this leads to differences in the magnitude of $h_{d,z}$ for the two skyrmion types. As illustrated in Figs. 3(b) and 3(c), measurements of the stray field above and below a skyrmion would provide a means to unambiguously identify the wall type.

Experiments are typically set up so that it is possible to obtain the stray field above but not below the spin texture. Further to this point, we compare stray field profiles above Néel walls of both chiralities and Bloch walls in Fig. 4. Figure 4 shows $H_{d,r}$, $H_{d,z}$ signals for Bloch and Néel walls of both chiralities in parts (a) and (b). Some of these lines represent the same data as presented in Fig. 3, however here, one explicitly sees the difference between Néel walls of clockwise versus counterclockwise chirality, and how they may possibly be discerned from one another using stray field analysis or the MFM signal (Fig. 4). In all three cases, the signal magnitude above the skyrmion wall differs substantially depending on the wall type. The shapes of the MFM profiles are very similar, independent of wall type, however, so if it is only possible to scan above the film, identification of the wall type/chirality

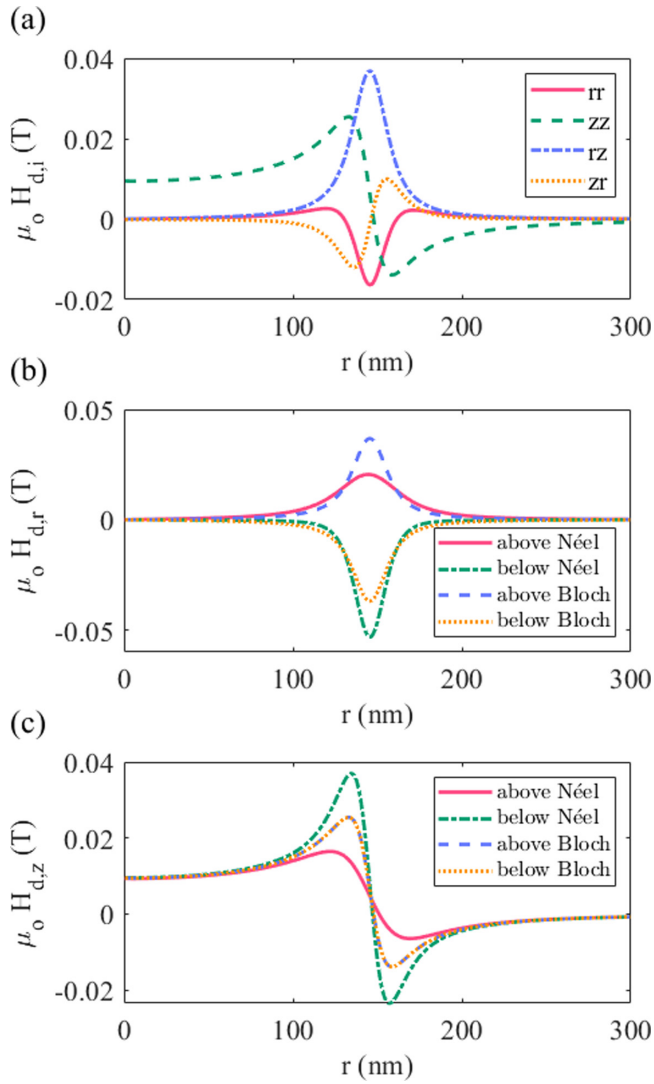


FIG. 3. (a) Matrix calculations of the stray field contributions at $h = 10$ nm above a Néel skyrmion with $R_{sk} = 145.7$ nm and $\Delta = 4.8$ nm. (b) $H_{d,r}$ and (c) $H_{d,z}$ are shown a distance of $h = 10$ nm above and below the surface of the magnetic layer, for a Néel ($\psi = 0$) and a Bloch ($\psi = \pi/2$) skyrmion.

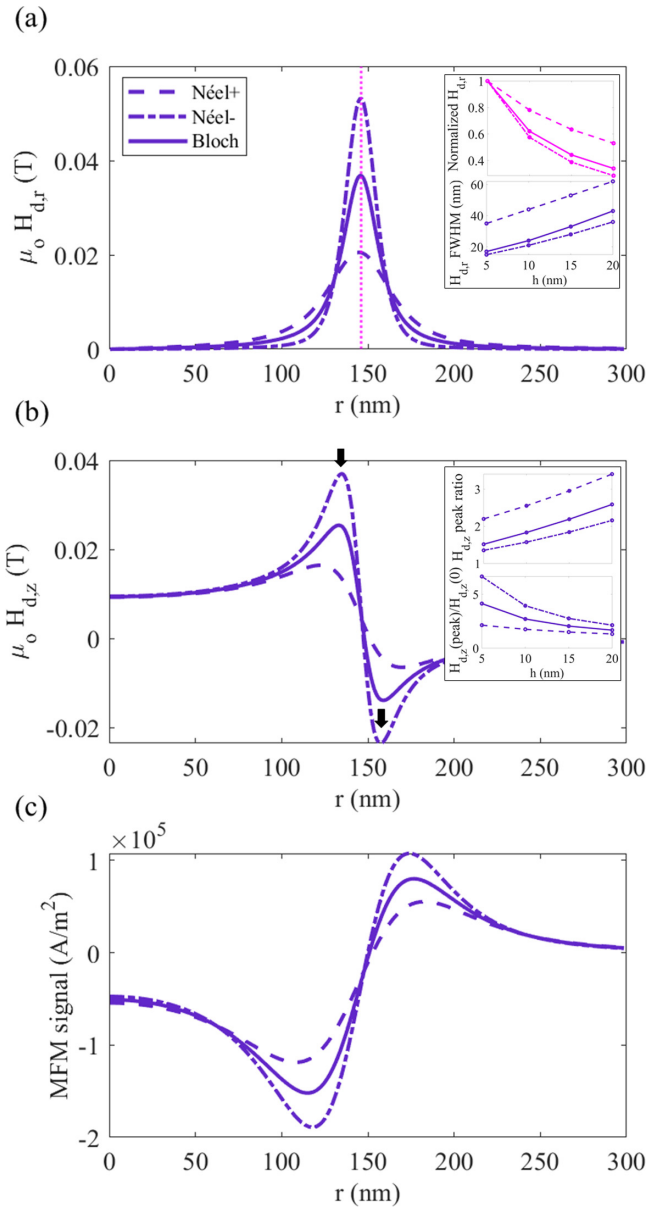


FIG. 4. (a) $r$ and (b) $z$ components of the stray magnetic fields above a magnetic skyrmion at $h = 10$ nm and (c) the corresponding MFM signal at $h = 50$ nm. Calculated profiles are shown for Néel skyrmions of both chiralities (dashed and dash-dot lines) where the sign in the legend indicates the sign of $m_r$ within the domain wall, and for a Bloch skyrmion (solid lines). The top inset of (a) shows $H_{d,r}$ at the maximum field value, marked in the main plot by the pink dotted line, vs $h$ where the $H_{d,r}$ values are normalized to the value at $h = 5$ nm for the corresponding wall type. The bottom inset of (a) shows the FWHM of $H_{d,r}$. In (b), the top inset shows the ratio of $H_{d,z}$ magnitudes at the peak and dip—shown by the black arrows in the main figure—and the bottom inset shows the ratio of $H_{d,z}$ at the positive peak to $H_{d,z}$ at $r = 0$ nm.

requires the ability to quantitatively measure the magnitude of the stray field above the skyrmion wall. As shown in the insets of Fig. 4, there are differences in how the magnitude of $H_{d,r}$ decreases as a function of $h$, in the full-width at half maximum (FWHM) of the $H_{d,r}$ profile (namely, the Néel+ wall has a wider stray field profile compared to the others for the same $\Delta$), and in the peak/dip ratios of the $H_{d,z}$ signals that can also be used to identify the domain wall type.

Obtaining the stray magnetic field from the magnetization is a linear problem [Eq. (21)], which suggests that linear inversion techniques may provide a means to obtain the magnetization profile directly from stray field measurements made at one or more heights. Indeed an inversion of the form $\mathbf{m} = \hat{G}_d^{-1}\mathbf{h_d}$ perfectly recovers the original magnetization profile from a calculated stray field profile, as expected. In order to determine if this approach will work on experimental data, we constructed synthetic datasets $\mathbf{h}_{dat}$ by adding 10% noise to stray field profiles. A single-height dataset, calculated for $h = 10$ nm, and a four-height dataset ($h = 5$, 10, 15, and 20 nm) were considered, where the first two heights of the four-height dataset for a Néel+ skyrmion are shown in Fig. 5(a). The magnetization profiles obtained by

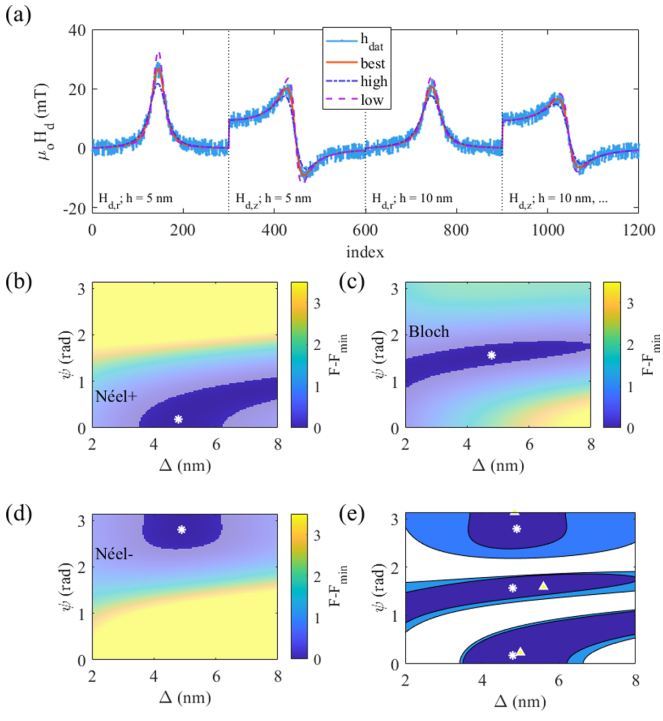


FIG. 5. (a) The first two heights ($h = 5$ and 10 nm) of a synthetic dataset $\mathbf{h}_{\rm dat}$ constructed using calculated $H_{d,r}$ and $H_{d,z}$ profiles at $h = 5$, 10, 15, and 20 nm for a Néel+ wall ($\psi = 0$) with $R_{\rm sk} = 145.7$ nm and $\Delta = 4.8$ nm with 10% white noise added. Best fits (solid lines) as well as high and low modeled profiles (dot-dashed and dashed) are also plotted. The high and low profiles correspond to two edge points of the dark best-fit parameter region in (b), namely, $(\psi, \Delta)$ of (0 rad, 6.35 nm) and (0 rad, 3.55 nm). The residual $F - F_{\rm min}$ as a function of $\Delta$ and $\psi$ for (b) a Néel+ skyrmion, (c) a Bloch skyrmion with $\psi = \pi/2$, and (d) a Néel- skyrmion are shown for the best fit $R_{\rm sk}$ values (all within 0.5 nm of the actual value, 145.7 nm). In all cases, the synthetic datasets were generated using $\Delta = 4.8$ nm with 10% white noise added. (e) Shaded-in contours for the four-height fits from (b)–(d) are displayed in dark blue, and the contours for corresponding single-height fits are shown in a lighter shade. The symbols (* and triangles) show the minima of $F$ for the four-height and single-height fits ($h = 10$ nm), respectively.

inverting $\mathbf{h}_{\rm dat}$ directly unfortunately bear little resemblance to the original $\mathbf{m}$. Two other linear inversion approaches, singular value decomposition and the conjugate gradient method, were tested and the latter provides a reasonable match to the magnetization profile, but the recovered $m_r$ is noisy and it is difficult to unambiguously identify the wall type from the inverted profiles.

Another approach that can be reliably used to obtain the wall type and width is illustrated in Fig. 5. Model magnetization profiles $\mathbf{m}_{\rm model}$, parameterized in terms of $R_{\rm sk}$, $\Delta$, and $\psi$, are constructed using Eq. (1) and a goodness of fit parameter is then calculated using

$$F = (\mathbf{h}_{\rm dat} - \hat{G}_d \mathbf{m}_{\rm model})^T (\mathbf{h}_{\rm dat} - \hat{G}_d \mathbf{m}_{\rm model}). \qquad (29)$$

The minimization of $F$ with respect to the three parameters can be done using any suitable optimization routine. Here we use a grid search technique. Figures 5(b)–5(d) show $F$ (colored contours) as a function of $\Delta$ and $\psi$ for synthetic datasets constructed using three different wall types, in all cases with $R_{\rm sk} = 145.7$ nm and $\Delta = 4.8$ nm, and Fig. 5(e) summarizes the contours that correspond to a reasonable fit for all three wall types. As shown in Fig. 5(e) the wall types are distinguishable when a single height is used (lighter contour), and additional heights can reduce the uncertainty in the recovered parameters (darkest shading). The best fit $R_{\rm sk}$ values are within <0.5 nm of the value used to construct the model datasets; based on a comparison of the modeled stray field profile and the synthetic dataset, the skyrmion radius is resolved to within 1–1.5 nm for a dataset with a 10% noise level.

The three-dimensional structure of spin textures is of increasing interest in magnetism, especially since recent measurements show that the wall type can evolve with depth in a multilayer film [6]. Figure 6 shows calculations of the stray magnetic field at $h = 10$ nm [panels (a) and (b)] and the MFM signal at $h = 50$ nm [panel (c)] above a skyrmion that penetrates through a three-layer magnetic thin film. Three layers with $L = 1$ nm are considered with 1-nm of space between each magnetic layer. The magnitude of the stray field and its gradient are larger for a skyrmion that has one Néel wall of each chirality and one Bloch wall (green and blue lines) as compared to a skyrmion that has Néel walls ($\psi = 0$, dashed purple lines) of the same chirality in all layers. There is also a difference in the magnitude of the stray magnetic field depending on whether the $\psi = 0$ Néel wall is on the top or the bottom, but this difference is small compared to the difference that arises based on whether or not there is a change in the wall type within the structure. As shown in the insets of Fig. 6, there are differences in how both components of the stray field magnitudes and the full-width at half maximum (FWHM) of the $H_{d,r}$ profile vary with $h$ that can be used to distinguish between the three considered spin distributions (N+/N+/N+, N+/B/N−, and N−/B/N+). These calculations indicate that MFM and nitrogen-vacancy (NV) magnetometry measurements, especially NV measurements made at several heights, may be used to discern the internal—and not just the surface—magnetic structures of multilayered skyrmions.

We discuss here the plausibility of using MFM and NV magnetometry to probe skyrmions in the context of our calculations. NV center magnetometry is an advanced and noninvasive technique that can be used to detect stray magnetic fields with a magnetic field sensitivity of a few nanotesla [28]. It should be possible to determine not only the number of layers of a particular type in a multilayer film but also the ordering of the wall types within the layers with this technique. MFM is also a highly sensitive technique and has been used to measure the magnetic moment of individual magnetic nanoparticles with diameters of 4.8 nm and with net moments as low as around $1.85 \times 10^{-20}$ A m$^2$ using an AC field-modulated approach [29]. It has also been used to image synthetic antiferromagnetic skyrmions that have a small net magnetic moment [30]. Tip-sample interactions can complicate the imaging of spin textures by MFM but with a careful analysis this can provide a means to quantify lateral interaction forces [18]. Based on the data shown in these papers, it should be possible to determine the number of layers of a particular type using MFM, but while determining the ordering

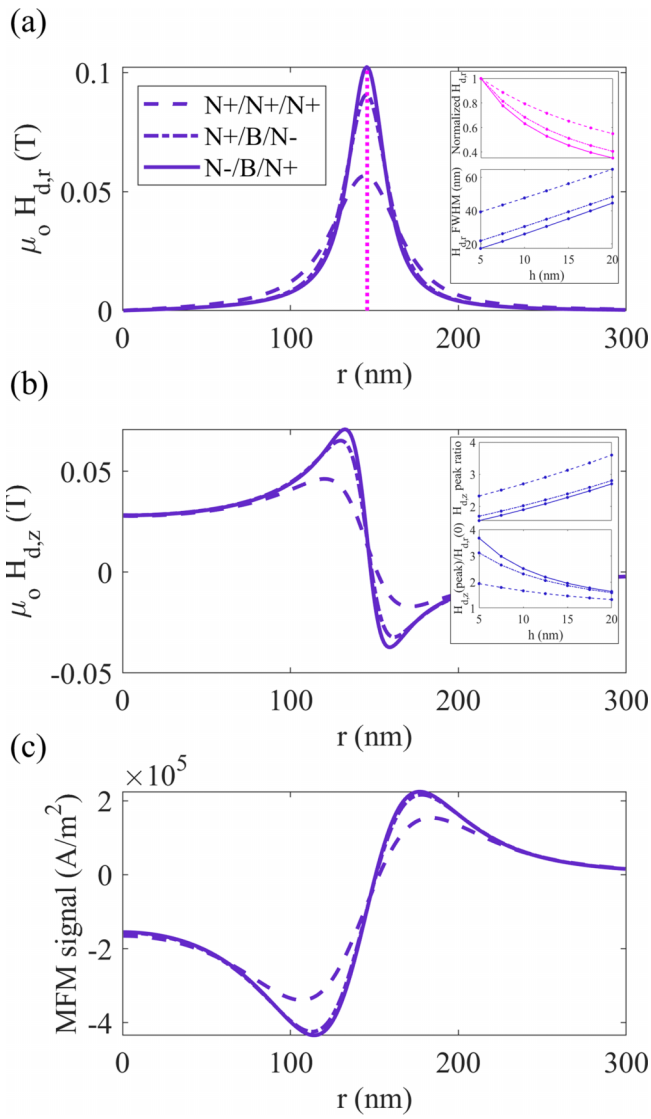


FIG. 6. (a) $r$ and (b) $z$ components of the stray magnetic fields at $h = 10$ nm and (c) the corresponding MFM signal at $h = 50$ nm for a set of skyrmions with in three magnetic layers of thickness $L = 1$ nm separated by 1 nm. The stray fields and MFM signals are shown for three cases: three Néel skyrmions with $m_r > 0$, and depth-dependent evolution of the wall type from top to bottom of Néel+/Block/Néel−, and Néel−/Bloch/Néel+. As in Fig. 4, the insets of (a) show $H_{d,r}$ at the maximum field value normalized to the value at $h = 5$ nm for the corresponding wall type and the FWHM of $H_{d,r}$ vs $h$, and the insets of (b) show the ratio of $H_{d,z}$ magnitudes at the peak and dip and the ratio of $H_{d,z}$ at the positive peak to $H_{d,z}$ at $r = 0$ nm vs $h$.

of the wall types within the layers may be possible it would likely be challenging. For both experimental techniques, the rapid calculations presented here will be useful for extracting information from measured data, with $R_{\rm sk}$, $\Delta$, and angle $\psi$ the only fit parameters to be adjusted.

## V. CONCLUSIONS

In conclusion, we have demonstrated a matrix-based semi-analytical method that can be used to obtain exact magnetic fields and field gradients above spin textures with cylindrical symmetry. For magnetic skyrmions, both the $r$ and the $z$ components of $\mathbf{H}_d$ differ considerably, by more than a factor of three in magnitude, depending on the skyrmion wall type and chirality, and the stray magnetic field also changes measurably when the wall type evolves with depth. Hence, this method can aid in unraveling the spin texture structure not just in single-layer structures but in more complex material stacks with 3D spin textures that vary through the thickness. We show how an approach that minimizes a goodness of fit parameter with respect to the three skyrmion parameters, $R_{\rm sk}$, $\Delta$, and $\psi$, a calculation that benefits from the rapid matrix-based method, provides a means to unambiguously identify the skyrmion wall type and obtain the uncertainty in the skyrmion parameters from fields measured above the sample. The presented approach is considerably faster than micromagnetic simulations, hence we anticipate that this method will be useful for analyzing and fitting data obtained using nitrogen vacancies in diamond and magnetic force microscopy, where for the latter it can easily be extended to incorporate the shape of the magnetic tip if needed. PYTHON code is provided to facilitate the use of this method in Ref. [27].

## ACKNOWLEDGMENTS

We acknowledge helpful discussions with Casey Chalifour, Jonathon Davidson, and Carla Quispe Flores. This work is supported by National Science Foundation DMR Grant No. 1709525. KLL was supported by a UCCS CRCW Award.

## APPENDIX A: DEFINITIONS OF MATRIX OPERATORS

The integral Green's function matrix operators $\hat{A}_{\alpha\beta}$ in Eq. (22) are $N \times N$ matrices with $r$ entries as rows, and $r'$ entries as columns, where each is discretized with a cell size of $\delta = \delta'$. The magnetization $\mathbf{m}(r')$ is a column vector of length $2N$ with the radial components ($N$ values) followed by the out-of-plane component (another $N$ values). The matrix operator $\hat{A}_{rr'}$ elements are

$$A_{rr',ij} = g_{rr'}(r_i, r'_j)\, r'_j\, \delta', \tag{A1}$$

where the distances are $r_i = (i - 1/2)\delta$ and $r'_j = (j - 1/2)\delta'$. Similar expressions are used for $g_{zz'}$, $g_{zr'}$, and $g_{rz'}$. Because $g_{rr'}$ changes rapidly near $r = r'$, the diagonal and near-diagonal terms of the demagnetization kernels were numerically integrated over each cell to obtain the average value within the cell

$$\bar{A}_{rr',ij} = \frac{1}{r'_j \delta'} \int_{r'_j-\delta'/2}^{r'_j+\delta'/2} g_{rr'}(r_i, r'_j)\, r'\, dr'. \tag{A2}$$

Note that the matrices $\hat{A}_{\alpha\beta}$ are not entirely symmetric because the integrated elements differ for $r < r'$ and $r > r'$. The cells with $r'_j = r'_N$ are integrated out to $\infty$ to approximate the effects of an extended thin film with a uniform magnetization, or out to the structure boundary for a finite cylindrical disk.

## APPENDIX B: SCALING OF THE MATRIX CALCULATION

The operation count to multiply a matrix with dimensions $m \times p$ by a vector of length $p$ is $2mp$. If $n$ is the length of each of the 1D $m_r$ and $m_z$ vectors, the length of $\mathbf{m}(r')$ is $2n$ and the

1D calculation will scale as $2(2n)(2n) = 8n^2$, assuming one magnetic layer and a single height. The demagnetization field calculation step in a 2D MuMax-type simulation can be set up as a matrix multiplication of the same form as Eq. (21), for example, by arranging the magnetization for a skyrmion in a film with a similar area and the same cell sizes as the 1D calculation as a vector of the form $[m_{x,1}, m_{y,1}, m_{z,1}, m_{x,2}, \dots]$ of length $3n^2$. The stray field operator matrix $\hat{G}_d$ is then a $3n^2 \times 3n^2$ matrix, and the operation count to obtain the 2D stray field at a single height is $18n^4$. Hence for the same $n$, the 2D calculation will take $2.25n^2$ times longer than a 1D calculation that covers a comparable area. This is significant, representing a factor of roughly $2 \times 10^5$, for the example shown in Fig. 5, which uses $n = 300$. Fast Fourier transform algorithms are often used in micromagnetics, in which case the 2D algorithm scales as $N \log_2(N)$ rather than $N^2$, where $N = 3n^2$ is the total number of cells. The time savings are then more modest but still significant especially for situations where multiple layers and/or measurement heights are considered.


[1] A. Fert, V. Cros, and J. Sampaio, Nat. Nanotechnol. **8**, 152 (2013).

[2] S. Rohart and A. Thiaville, Phys. Rev. B **88**, 184422 (2013).

[3] S. Woo, K. Litzius, B. Krüger, M. Y. Im, L. Caretta, K. Richter, M. Mann, A. Krone, R. M. Reeve, M. Weigand, P. Agrawal, I. Lemesh, M. A. Mawass, P. Fischer, M. Kläui, and G. S. Beach, Nat. Mater. **15**, 501 (2016).

[4] C. Moreau-Luchaire, C. Moutafis, N. Reyren, J. Sampaio, C. A. Vaz, N. Van Horne, K. Bouzehouane, K. Garcia, C. Deranlot, P. Warnicke, P. Wohlhüter, J. M. George, M. Weigand, J. Raabe, V. Cros, and A. Fert, Nat. Nanotechnol. **11**, 444 (2016).

[5] T. Dohi, S. DuttaGupta, S. Fukami, and H. Ohno, Nat. Commun. **10**, 5153 (2019).

[6] W. Li, I. Bykova, S. Zhang, G. Yu, R. Tomasello, M. Carpentieri, Y. Liu, Y. Guang, J. Gräfe, M. Weigand, D. M. Burn, G. van der Laan, T. Hesjedal, Z. Yan, J. Feng, C. Wan, J. Wei, X. Wang, X. Zhang, H. Xu, C. Guo, H. Wei, G. Finocchio, X. Han, and G. Schütz, Adv. Mater. **31**, 1807683 (2019).

[7] N. Kent, N. Reynolds, D. Raftrey, I. T. Campbell, S. Virasawmy, S. Dhuey, R. V. Chopdekar, A. Hierro-Rodriguez, A. Sorrentino, E. Pereiro, S. Ferrer, F. Hellman, P. Sutcliffe, and P. Fischer, Nat. Commun. **12**, 1562 (2021).

[8] P. Fischer, IEEE Trans. Magn. **51**, 800131 (2015).

[9] J. Miao, P. Ercius, and S. J. Billinge, Science **353**, aaf2157 (2016).

[10] S. Zhang, G. Van Der Laan, J. Müller, L. Heinen, M. Garst, A. Bauer, H. Berger, C. Pfleiderer, and T. Hesjedal, Proc. Natl. Acad. Sci. USA **115**, 6386 (2018).

[11] C. Phatak, A. K. Petford-Long, and M. De Graef, Curr. Opin. Solid State Mater. Sci. **20**, 107 (2016).

[12] S. D. Pollard, J. A. Garlow, J. Yu, Z. Wang, Y. Zhu, and H. Yang, Nat. Commun. **8**, 14761 (2017).

[13] S. Hong, M. S. Grinolds, L. M. Pham, D. Le Sage, L. Luan, R. L. Walsworth, and A. Yacoby, MRS Bull. **38**, 155 (2013).

[14] L. Rondin, J. P. Tetienne, S. Rohart, A. Thiaville, T. Hingant, P. Spinicelli, J. F. Roch, and V. Jacques, Nat. Commun. **4**, 2279 (2013).

[15] J. P. Tetienne, T. Hingant, L. J. Martínez, S. Rohart, A. Thiaville, L. H. Diez, K. Garcia, J. P. Adam, J. V. Kim, J. F. Roch, I. M. Miron, G. Gaudin, L. Vila, B. Ocker, D. Ravelosona, and V. Jacques, Nat. Commun. **6**, 6733 (2015).

[16] O. Kazakova, R. Puttock, C. Barton, H. Corte-León, M. Jaafar, V. Neu, and A. Asenjo, J. Appl. Phys. **125**, 060901 (2019).

[17] F. Casola, T. Van Der Sar, and A. Yacoby, Nat. Rev. Mater. **3**, 17088 (2018).

[18] A. Yagil, A. Almoalem, A. Soumyanarayanan, A. K. Tan, M. Raju, C. Panagopoulos, and O. M. Auslaender, Appl. Phys. Lett. **112**, 192403 (2018).

[19] C. Flores, A. Stuart, K. Buchanan, and K. Livesey, J. Magn. Magn. Mater. **513**, 167164 (2020).

[20] B. Göbel, I. Mertig, and O. A. Tretiakov, Phys. Rep. **895**, 1 (2021).

[21] C. Quispe Flores, C. Chalifour, J. Davidson, K. L. Livesey, and K. S. Buchanan, Phys. Rev. B **102**, 024439 (2020).

[22] F. Büttner, I. Lemesh, and G. S. Beach, Sci. Rep. **8**, 4464 (2018).

[23] K. Y. Guslienko, W. Scholz, R. W. Chantrell, and V. Novosad, Phys. Rev. B **71**, 144407 (2005).

[24] J. D. Jackson, *Classical Electrodynamics*, 3rd ed. (Wiley, New York, 1998), p. 832.

[25] M. T. Hanson and I. W. Puja, Q. Appl. Math. **55**, 505 (1997).

[26] A. Vansteenkiste, J. Leliaert, M. Dvornik, M. Helsen, F. Garcia-Sanchez, and B. Van Waeyenberge, AIP Adv. **4**, 107133 (2014).

[27] See Supplemental Material at http://link.aps.org/supplemental/10.1103/PhysRevB.105.144430 for Python code of the matrix method.

[28] J. R. Maze, P. L. Stanwix, J. S. Hodges, S. Hong, J. M. Taylor, P. Cappellaro, L. Jiang, M. V. Dutt, E. Togan, A. S. Zibrov, A. Yacoby, R. L. Walsworth, and M. D. Lukin, Nature (London) **455**, 644 (2008).

[29] X. Li, W. Lu, Y. Song, Y. Wang, A. Chen, B. Yan, S. Yoshimura, and H. Saito, Sci. Rep. **6**, 22467 (2016).

[30] W. Legrand, D. Maccariello, F. Ajejas, S. Collin, A. Vecchiola, K. Bouzehouane, N. Reyren, V. Cros, and A. Fert, Nat. Mater. **19**, 34 (2020).